ACS OMEGA

Open Access

http://pubs.acs.org/journal/acsodf

Article

Coupling Process between Droplet and Iron Investigated by Reactive Molecular Dynamics Simulations

Hang Dong,* Can Zhao, Na Kong, Yu Zhou, and Jianping Zhou

Cite This: *ACS Omega* 2024, 9, 20410−20424

Read Online

ACCESS | Metrics & More | Article Recommendations

ABSTRACT: The droplet-to-iron electrochemical reaction is common in nature and industrial production, and it causes damage to the economy, safety, and the environment. The electrochemical reaction of droplet-to-iron is a coupling process of wetting and corrosion. Presently, investigations into electrochemical reactions mainly focus on the corrosions caused by a solution, and wetting is rarely considered. However, for the droplet-to-iron electrochemical reaction, the mechanism of charge transfer in the process is still unclear. In this paper, a reactive molecular dynamics simulation model for the droplet-to-iron electrochemical reaction is developed for the first time. The electrochemical reaction of droplet-to-iron is studied, and the interaction between droplet wetting and corrosion on iron is investigated. The effects of temperature, electric field strength, and salt concentration on the electrochemical reaction are explored. Results show that droplet wetting on the iron surface and the formation of a single-molecular-layer ordered structure are prerequisites for corrosion. The hydroxyl radicals that penetrate the ordered structure acquire electrons from iron atoms on the substrate surface under the action of Coulomb forces and form iron-containing oxides with these iron atoms. The corrosion products and craters lead to a reduced droplet height, which promotes droplet wetting on iron and further intensifies the droplet-to-iron electrochemical reaction.

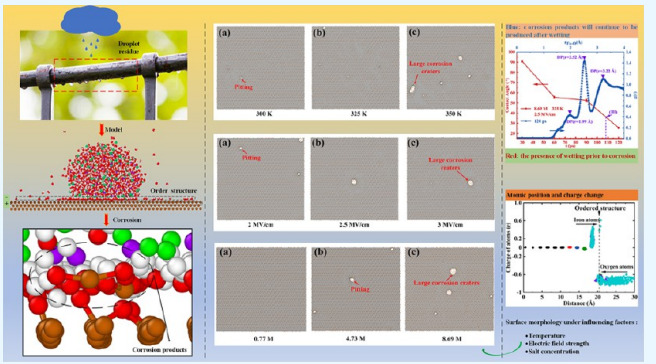

1. INTRODUCTION

The reaction of an electrolyte with a iron surface is the main prerequisite for the research of electrochemical reactions.[1] Among the electrochemical reactions, corrosion and corrosion protection cause the most damage and account for more than 3% of the global GDF.[2,3] The reaction of an electrolyte with an iron surface encompasses the electrochemical reaction of solution and droplet-to-iron. Electrochemical reaction between electrolyte and iron surface is a spontaneous behavior that pollutes the environment, degrades performance, and shortens the service life of materials.[4] Specifically, it is reflected in ships, roads and bridges, aerospace, and other fields.[5] Unlike the electrochemical reaction of solution-to-iron, the droplet-to-iron reaction is a coupling process of wetting and corrosion. Moreover, droplets are more common in natural interactions, such as droplets with corrosive ions that remain on buildings after rain and seawater droplets left on ships. The droplet is a solution component; thus, the electrochemical reaction of a droplet can provide a basis for the electrochemical reaction of the solution. Furthermore, the electrochemical reaction of droplet-to-iron can provide reference values for other systems where chemical reactions occur at the interface, e.g., electrochemical processing,[6,7] material joining, film growth,[8−10] disease detection, and diagnosis.[11,12] A good grasp of the electrochemical reaction of droplet-to-iron is essential for saving resources, improving the environment, and creating wealth. For the complex dynamic processes at the electrolyte/solid surface that are difficult to characterize experimentally, capturing the interfacial reactions with the help of molecular dynamics also aids in experimental studies. With the improvement of computational power, the simulation study of molecular dynamics of reactions based on the REAXFF force field has also become a hot spot to study the electrochemical reactions on the electrolyte/solid surface.

Recently, reactive molecular dynamics simulations (ReaxFF-MD) have been conducted to investigate the complex electrochemical reaction of the solution. Li et al.[13] investigated the effect of sodium chloride solutions on γ-FeOOH structures. Chloride ions were found to attack the γ-FeOOH structure and promote the onset of a solution electrochemical reaction. Assowe et al.[14] used a pure aqueous solution to interact with nickel and found that the thickness of the oxide

Received: February 7, 2024
Revised: April 16, 2024
Accepted: April 19, 2024
Published: April 26, 2024

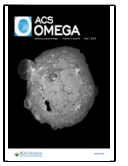

film increases linearly with increasing electric field strength. Jeon et al.[15,16] have successfully studied the interaction of copper substrates with chlorine in water and the adsorption and transport of chlorine ions in water in copper oxide films.

A large number of iron related studies have been carried out by scholars. Du et al.[17] investigated carbon steel's electrochemical reaction, charge distribution, and oxide growth under salt spray by using the ReaxFF-MD method. The rate before 600 ps was determined by the chemical reaction rate, after which the electrochemical reaction rate depended on the diffusion rate of the electrons. Subbaraman et al.[18] studied the early growth of iron oxides with different surface orientations. In their study, it was found that the development of the oxides conforms to the logarithmic law. Farzi et al.[19] have investigated the corrosion behavior of carbon steel in water and acidic solutions. The results of quantum mechanical calculations showed that the more stable products in water and acidic solutions are FeO_4H_8 and FeO_5H_9, respectively. Huang et al.[20] improve the reactive force field of Fe−H_2O and examine the corrosion of Fe (100) and Fe (110) in supercritical water.

A simulation of the liquid-to-iron interaction by reactive force fields can better disclose the electrochemical reaction, especially in the presence of liquids with corrosive ions. In these studies, the simulation results often match the theoretical model, thus reflecting the reasonableness and reliability of the simulation. However, the simulation studies mainly focused on the electrochemical reaction of metals by solutions. Droplet-to-iron systems are relatively common in life and also cause significant losses, but have rarely been studied at the atomic level. How the wetting and corrosion interact in the droplet-to-iron electrochemical reaction is ambiguous. The mechanism of charge transfer during droplet-to-iron electrochemical reaction is still unknown.

In this work, a model for droplet-to-iron electrochemical reaction is established for the first time. The electrochemical reaction of droplet-to-iron is studied at the atomic level by ReaxFF-MD simulations, and the interaction between droplet wetting and corrosion on iron is investigated. Charge and atomic position changes are tracked; the extension of the dissolved region on the iron surface is recorded, and the number of atoms in different phases is counted. The effects of three factors on droplet-to-iron electrochemical reaction are explored by varying the temperature, electric field strength, and salt concentration.

2. MODEL AND METHOD

2.1. ReaxFF Force Field. The ReaxFF force field is an empirical force field that is specifically designed to describe chemical reactions that react with the formation and breaking of chemical bonds through molecular dynamics. Unlike the conventional nonreactive force field, the reactive force field does not need to fix the connectivity between atoms within a molecule. It determines the connectivity of atoms by calculating the bond order between two atoms. Therefore, the expression of the bond order BO_{ij} in the reactive force field, as shown in Equation 1, is significant.

$$BO'_{ij} = BO^{\sigma}_{ij} + BO^{\pi}_{ij} + BO^{\pi\pi}_{ij} = \exp\left[p_{bo1}\cdot\left(\frac{r_{ij}}{r^{\sigma}_{o}}\right)^{p_{bo2}}\right] + \exp\left[p_{bo3}\cdot\left(\frac{r_{ij}}{r^{\pi}_{o}}\right)^{p_{bo4}}\right] + \exp\left[p_{bo5}\cdot\left(\frac{r_{ij}}{r^{\pi\pi}_{o}}\right)^{p_{bo6}}\right] \quad (1)$$

BO'_{ij} can be obtained directly from the interatomic distance r_{ij}, and its contribution to the bond order contains σ bonds (P_{bol} and P_{bo2}), π bonds (p_{bo3} and p_{bo4}), and double-π bonds (p_{bo5} and p_{bo6}).

The simulation of the Fe−H_2O system is performed based on the ReaxFF-MD method developed by van Duin et al.[21] The total energy is expressed in bond order, as shown in Equation 2, and bond order is used to describe the strength of the chemical bonds between atoms. The interatomic interactions are calculated by stretching, bending, and twisting the bonds within the molecule.

$$E_{system} = E_{bond} + E_{over} + E_{under} + E_{val} + E_{tor} + E_{lp} + E_{H\text{-}bond} + E_{vdWaals} + E_{Coulomb} \quad (2)$$

In Equation 2, except for E_{bond}, which is the bond energy, E_{over} and E_{under} are penalized over and undercoordinated atoms, respectively. E_{val}, E_{tor}, E_{pl}, $E_{H\text{-}bond}$, $E_{vdWaals}$, and $E_{Coulomb}$ are the valence angle energy, torsion energy, lone pair energy, hydrogen bond energy, van der Waals energy, and Coulomb energy, respectively. In the ReaxFF system, the most computationally expensive and time-consuming charge distribution methods are used for atoms, namely, the Qeq method,[22] which makes the individual atomic charges and their electrostatic energies change dynamically with time.

Aryanpour et al.[23] and Rahaman et al.[24] developed C, H, O, and Cl parameters and successfully simulated the reaction mechanism of chlorides with metals such as Fe and Cu. Dormohammadi et al.[25] studied the electrochemical reaction model of pure water on Fe for different applied electric fields and temperatures. They also compared the surface formation energy and water adsorption energy of the Fe(110) surface by performing DFT calculations to verify the feasibility of their parameters.[26] Psofogiannakis et al.[27] added the reaction between sodium ions and other parameters to the C, H, O, and Cl systems.

In this paper, Reaxff is chosen as the force field in consideration of the electrochemical reaction. The force field parameters for simulating droplet-to-iron electrochemical reaction are derived from ref 26, where the main objective of Dormohammadi et al. was to simulate the chloride ion-induced iron depassivation process of pure iron in a highly alkaline environment (0.316 M sodium hydroxide solution, i.e., pH = 13.5) using ReaxFF-MD.

2.2. Simulation Settings. The simulation system established in this paper is shown in Figure 1. The green, purple, white, red, and reddish-brown colors represent sodium, chloride, hydrogen, oxygen, and iron atoms, respectively. The initial model is modeled with the help of PACKMOL software,[28] and MD simulations are performed using the Large-scale Atomic/Molecular Massively Parallel Simulator[29] and finally visualized in OVITO software.[30]

Before the initial model is built, the sodium chloride droplet and the iron metal plate are optimized in the PACKMOL

https://doi.org/10.1021/acsomega.4c01236
ACS Omega 2024, 9, 20410−20424

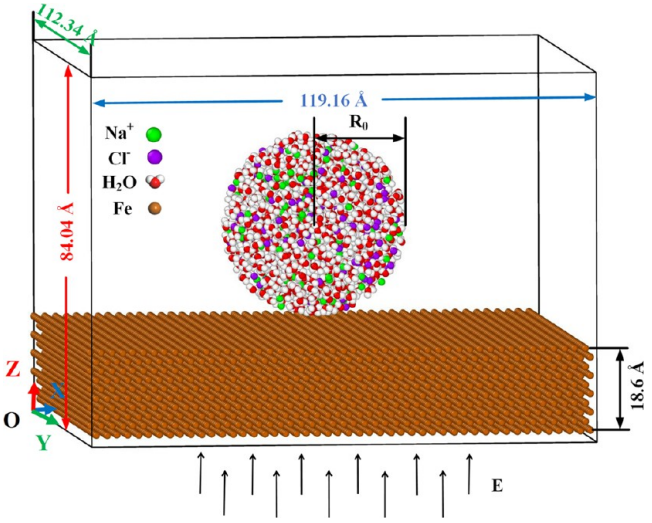

Figure 1. Schematic of the simulation system.

software package with a distance tolerance of 2 Å.[31] Before the sodium chloride droplet and the iron metal plate are combined, the sodium chloride droplet and the iron metal plate must be relaxed separately to make the model more reasonable and to optimize the structure. For 23040 iron atoms oriented (100) along the surface normal, the iron metal plate is 18.6 Å thick. First, a random number is specified such that all atomic velocities can satisfy a Gaussian distribution at 300 K, and the Verlet algorithm integrates the Newtonian equations of motion. Then, the conjugate gradient method is used, and the convergence tolerances of energy and force are both set to 10^{-10} kcal/mol. The maximum number of iteration steps is 10^4 and the ultimate energy estimate is 5000 kcal/mol. In addition, the bottom four layers of atoms of the iron substrate are immobilized throughout the relaxation and dynamics to prevent the iron from floating up and down, which would affect the simulation results. The iron substrate does not have a significant volume change during the kinetic process, and the NVT system is also used for the relaxation of iron in refs 14, 17, and 21. Therefore, the NVT system is finally chosen for relaxation. The NVT ensemble is equilibrated for 20 ps at a temperature of 300 K. For a sodium chloride droplet with a radius of R_0 = 20 Å, the same energy minimization approach is used, but the convergence tolerances for energy and force are set to 10^{-6} and 10^{-8} kcal/mol, respectively. Relaxation is performed for 20 ps at a temperature of 300 K for the NPT ensemble.

The relaxed combination of the two models is placed in a box with a size of 119.16 × 112.34 × 84.04 $Å^3$ consisting of an iron and a sodium chloride droplet 5 Å from the iron. The number of molecules for different concentrations of sodium chloride droplets is shown in Table 1. A total of 1106 water molecules and the droplet concentration is varied by adjusting the amount of sodium chloride. Jeon et al.[16] concluded that obtaining significant results on the time scale for low chloride concentrations is difficult. Thus, in the current paper, the concentration gradient is set at a considerable distance and as close as possible to the concentration stated by Jeon et al.

Table 1. Number of Molecules in Sodium Chloride Droplet

Case	No. of water molecules	No. of NaCl	Salt concentration (M)
1	1106	15	0.77
2		95	4.73
3		174	8.69

An upward electric field is applied perpendicular to the direction of the iron with the electric field strength being adjusted (2, 2.5, and 3 MV/cm). Reactive molecular dynamics simulations can reveal the dynamic laws at the atomic scale. The simulation model is usually established in nanoscale due to the limitation in computational resources and is different from the actual experiment in spatial scales.[32] The electric field strength applied in this work is also higher than that in the actual experiment. The order of the electric field strength magnitude applied in this work is commonly used in the field of reactive molecular dynamics simulation, and the corresponding simulation results have good agreement with experimental results.[14,25] For the simulated box, periodic boundary conditions are used in the x- and *y*-directions.[20] In contrast, fixed boundary conditions are imposed in the *z*-direction and a bouncing wall is set at the upper and lower boundaries of the *z*-axis to restrict the action of the water molecules.

In this work, the electrochemical reaction of a droplet at different temperatures (300, 325, and 350 K) and the variation of contact angle and product formation are also investigated aside from the electric field strength and salt concentration. During the simulations, the NVT ensemble is used to maintain the system temperature by using a Nosé−Hoover thermostat with a damping constant of 50 fs. The whole simulation occurs within 200 ps with an integration step of 0.2 fs, and the information on the molecules' position and the system's thermodynamic information output every 1000 fs are used for analysis.

3. RESULT AND DISCUSSION

3.1. Droplet-to-Iron Electrochemical Reaction. The droplet-to-iron electrochemical reaction at a temperature of 325 K, an electric field strength of 2.5 MV/cm, and a salt concentration of 8.69 M is shown in Figure 2. Droplet evaporation takes place throughout the electrochemical reaction because of the vapor pressure difference between the gas and liquid.[33] Wu et al.[34] discussed an evaporation model where a portion of the water molecules in the droplet is reflected or captured, and the other portion escapes to the gas phase, i.e., evaporation. Therefore, the water molecules in the environment of this paper are defined as evaporated water molecules.

Figure 2 shows that the droplet-to-iron electrochemical reaction under the action of the applied electric field will go through three stages. Figures. 2 a and b show the first stage. The initial distance between the droplet's lower end and the iron surface is 5 Å. The water molecules around the droplet move toward the iron and adsorb on the surface of the iron substrate, as shown by the arrows in Figure 2a. Suganuma et al.[35] speculated on the presence of van der Waals forces during wetting and found significant changes in wetting by varying the forces between the droplet and the surface. Moreover, the droplet is electrically neutral and does not move in the presence of an electric field. Thus, van der Waals forces are considered to be the forces that hold the droplet and the substrate close to each other. The van der Waals force between the droplet and the substrate causes the droplet to gradually approach the substrate and spread out on the substrate. Under

https://doi.org/10.1021/acsomega.4c01236
ACS Omega 2024, 9, 20410−20424

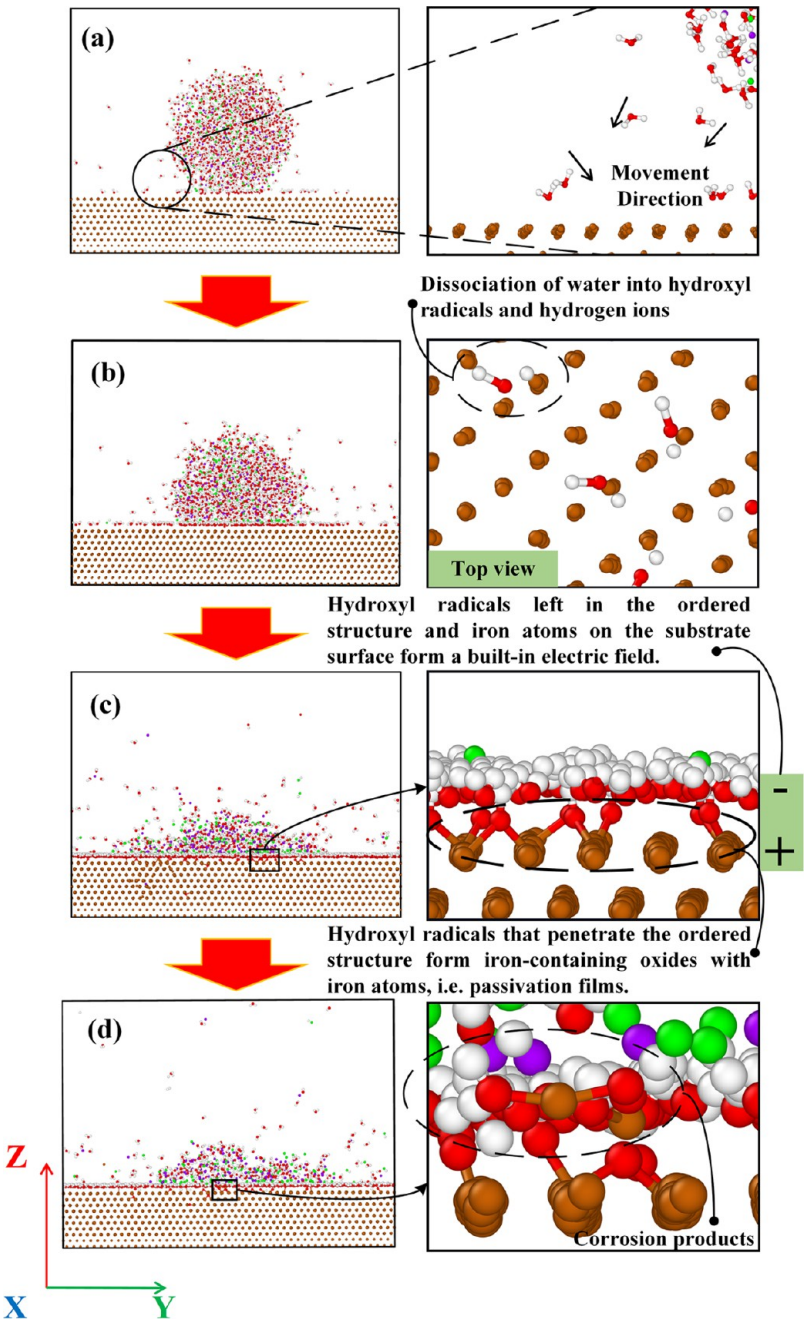

Figure 2. Simulation of the droplet-to-iron electrochemical reaction. (a) and (b) Electrochemical reaction stage 1. (c) Electrochemical reaction stage 2. (d) Electrochemical reaction stage 3.

van der Waals forces, neither chemical reactions occur, nor do substances change their original properties.

During the wetting process, water molecules in the droplet and water molecules in the environment form a single-molecular-layer ordered structure on the surface of the iron substrate, where the water molecules dissociate, and the H−O bonds are broken. The expression for the dissociation of water is $H_2O \rightarrow OH^- + H^+$. The dissociated hydroxyl radicals and hydrogen ions can be seen in the top view of Figure 2b. In the ordered structure, the oxygen atom faces the iron and the hydrogen atom moves away from the iron. The detailed arrangement of ordered structures was also studied by Li et al.,[36] whose simulation results showed that the oxygen and hydrogen atoms undergo a process from random to ordered distribution. Wang et al.[37] pointed out that this ordered distribution at the interface promotes efficient interfacial charge transfer. The specific charge transfer mechanism is illustrated in Figure 3 and will be discussed below.

After some time, the droplet-to-iron electrochemical reaction enters the second stage (Figure 2c). Partial hydroxyl radicals penetrate the single-molecular-layer ordered structure and are connected to the iron atoms in the form of a chemical bond, and the chloride ions are on the surface of the single-molecular-layer ordered structure.

The third stage is shown in Figure 2d. Under the influence of chemical bonding forces, the hydroxyl radicals form iron-containing oxide with iron atoms, leave the iron upper surface, and finally enter the single-molecular-layer ordered structure.

https://doi.org/10.1021/acsomega.4c01236
ACS Omega 2024, 9, 20410−20424

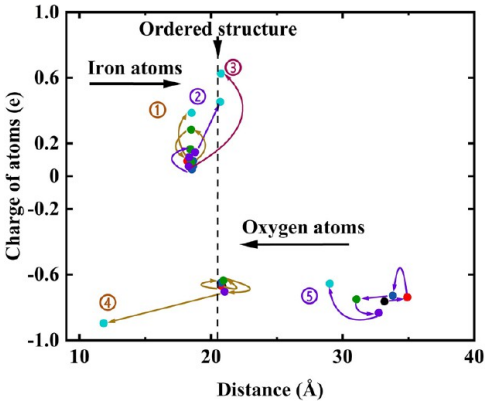

Figure 3. Charge and position changes of iron and oxygen atoms with time. Electrochemical reaction stage 1: black and red. Electrochemical reaction stage 2: blue, green, and purple. Electrochemical reaction stage 3: cyan.

Chemical bonding forces are greater than van der Waals forces, thereby promoting pulling of the iron atoms away from the substrate surface. The detachment of the iron atoms from the substrate surface results in pitting, which loosens the dense iron structure, thus accelerating the diffusion of the hydroxyl radicals and the further corrosion of the iron. The reaction expression is $Fe \rightarrow Fe^{n+}+ne^{-}$. Over time, the pitting develops into large areas of corrosion. The resultant pitting and large corrosion craters are occupied by the single-molecular-layer ordered structure, which promotes the wetting of the droplet on the substrate surface.

The charge and position changes of some iron and oxygen atoms are traced, as shown in Figure 3, to further verify the charge transfer process. The three traced atoms with positive charges are the iron atoms, while the two with negative charges are the oxygen atoms. The dashed line in Figure 3 represents the lower surface of the single-molecular-layer ordered structure, with the iron on the left side and the droplet on the right side of the dashed line. The horizontal coordinates are the coordinate positions along the *z*-axis, and the vertical coordinates represent the magnitude of the atomic charges. Cyan color represents the third stage of electrochemical reaction, while blue, green, and purple colors represent the changes in atomic charge and position at different time steps of the second stage of electrochemical reaction, respectively. Black and red colors indicate two different time steps in the first stage of the electrochemical reaction. The different time steps are separated by the same time. Oxygen (from hydroxyl radicals) and iron atoms near the single-molecular-layer ordered structure eventually move from the black to the cyan position and penetrate the ordered structure. During this time, the absolute value of the iron charge increases.

This result can be explained by two aspects. First, as the simulation proceeds, hydroxyl radicals accumulate in the ordered structure. The hydroxyl radicals are then subjected to electric field force and Coulomb force and collide with the particles. The energies of some hydroxyl radicals increase, and they can penetrate the ordered structure. Jung et al.[38] reported that the adhesion and rebound of the particles are the outward manifestation of the energy exchange during the particle collision. This result further confirms that the mutual collisions and energy exchanges between atoms in Figure 3 lead to changes in atomic positions. Figure 3 also indicates that the changes in atomic positions accompany the droplet-to-iron electrochemical reaction. Second, the hydroxyl radicals that penetrated the ordered structure have stronger Coulomb forces acting on the iron atoms on the surface than those below the surface of the substrate. Then, the iron atoms on the substrate surface lose electrons, which are transferred to the penetrated hydroxyl radicals, manifested as an increase in the absolute value of the charges of the iron and oxygen atoms. The transfer of electrons from the iron atom to the hydroxyl radical is consistent with the transfer of electrons from the solid side to the liquid side as described by Lin et al.[39] Meanwhile, a built-in electric field forms between the hydroxyl radicals that remain in the ordered structure and positively charged iron atoms that have lost electrons on the substrate surface (Figure 2c). The built-in electric field can promote the movement of penetrated hydroxyl radicals and accelerate the corrosion. Obviously, a high valence state of a multivalent metal, corresponds to a higher strength of the built-in electric field that will be formed.

Contact angle measurement can analyze the degree of droplet wetting on the metal. In general, the value of the contact angle is influenced by the free energy of the solid surface, which is reflected in the magnitude of the molecular forces on the solid surface and the arrangement and structure of the surface molecules. For established metals, the solid surface free energy is often determined and the wetting state does not change substantially with time after the system is in equilibrium. However, chemical interactions occur during the droplet-to-iron electrochemical reaction. The solid surface morphology changes, with pitting and even large areas of corrosion.[40,41] The red curve in Figure 4 represents the

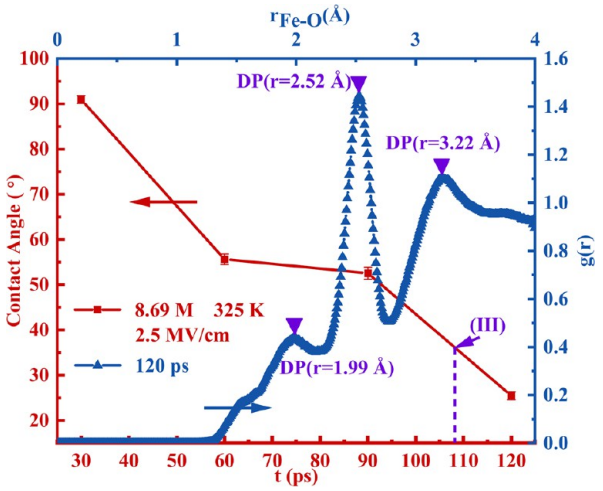

Figure 4. Variation of droplet contact angle with time and pairwise distribution function of Fe−O interactions.

variation of contact angle with time. The contact angle of the droplet is measured three times, and the mean and standard deviation are taken to obtain the change in the contact angle of the droplet during the coupling process. When the time reaches 108.2 ps (droplet-to-iron electrochemical reaction enters the third stage as shown at [III] in the Figure), the contact angle is reduced to about 36°, and then only at this point do the corrosion products begin to be generated. This behavior indicates that wetting occurs before corrosion. The formation of the single-molecular-layer ordered structure caused by the wetting of a droplet on the iron surface is a prerequisite for corrosion occurrence. The influence of wetting

https://doi.org/10.1021/acsomega.4c01236
ACS Omega 2024, 9, 20410−20424

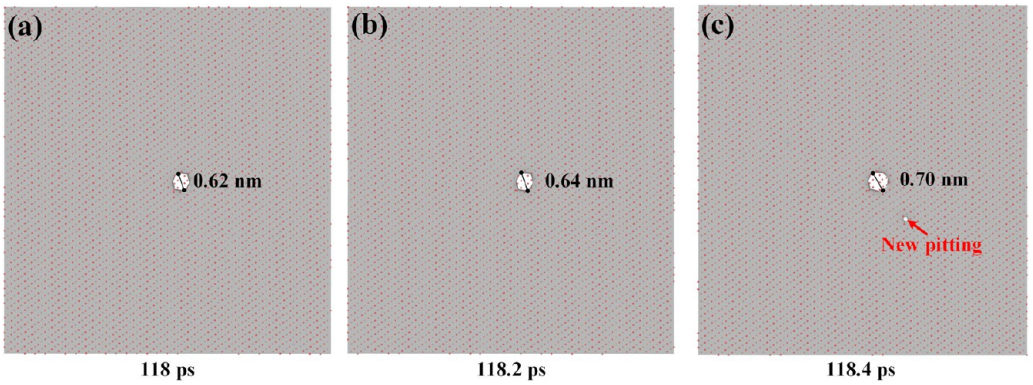

Figure 5. Growth of corrosion craters over time: (a) 118 ps, (b) 118.2 ps, (c) 118.4 ps.

on the droplet corrosion is mainly reflected in the formation of the single-molecular-layer ordered structure described above. A shorter time to form the ordered structure corresponds to a faster occurrence of corrosion. The influence of corrosion on wetting is mainly reflected in two aspects. First, the products generated by the corrosion appear in the droplet, reducing the number of interactions of droplet water molecules. Second, the appearance of corrosion craters enlarges the exposed area of the iron substate, and more hydroxyl radicals can contact and fill the craters. Therefore, the droplet height decreases, and the contact angle decreases (Figure 4).

The radial distribution function (RDF) $g(r)$ calculates the probability of distribution of other particles in the space around it by giving the particle coordinates, as shown in Equation 3

$$g(r) = \frac{dN}{\rho 4\pi r^2 dr} \tag{3}$$

Where ρ is the system density, r is the distance from the particle to the central particle, and dN is the number of particles between r and $r + dr$.

The pairwise distribution function (PDF) is a particular case of the RDF, which is usually used in molecular dynamics simulations with charge distribution maps to analyze corrosion products. The PDF in the droplet-to-iron electrochemical reaction is shown in Figure 4 with a blue curve, where the first dominant peak (DP) indicates the minimum distance between atoms. The purple triangles in Figure 4 mark the respective peak PDF values obtained by the calculation. The first DP in Figure 4 corresponds to the Fe−O bond length of about 1.99 Å, which is relatively close to the RDF value of magnetite, indicating the possible presence of Fe_3O_4 in the corrosion products.

Generally, corrosion is a process of generation and dissolution of passivation film.[42] In this droplet-to-iron electrochemical reaction simulation, the droplet first reacts with the iron atoms on the surface of the pure iron substrate to form an iron-containing oxide (passivation film),[16] as shown in Figure 2c. As the reaction proceeds, iron atoms are dragged from the substrate surface by the chemical bonding of oxygen atoms, causing damage to the passivation film and forming corrosion products. The formed corrosion products enter the single-molecular-layer ordered structure as shown in Figure 2d. Therefore, this simulation can reflect the electrochemical reaction of passivation film generation and dissolution well. The same pure iron substrate model has been used in reactive molecular dynamics simulations of solution electrochemical reaction, such as those conducted by Dormohammadi and Subbaraman et al.[18,25] Their simulations contained passivation film formation and dissolution processes and agreed well with the experimental results. The RDF is also consistent with the simulations by Dormohammadi et al. Among the corrosion products that they simulated, the minerals that had dominant peak positions of PDFs are wustite (1.65 Å), hematite (1.7 Å), and magnetite (2.0 Å). As described previously, the generation of corrosion products in Figure 4 can verify the corrosion affecting wetting.

Figure 5 shows the growth of corrosion craters, where the thickness of the intercepted surface layers is all 2 Å. The annular hole indicated by the arrow is pitting, and the flaky areas are large corrosion craters. The large corrosion crater in Figure 5a is where corrosion occurs first. When the corrosion crater reaches a certain size, new pitting will occur (Figure 5c), thus confirming that corrosion craters will evolve and undergo derivation, development, and convergence.

Table 2 compares the main essential points between other studies and this work. The comparison is conducted in four main parts: model application, electrochemical reaction, charge transfer mechanism, and coupling process. First, the pure iron substrate model is utilized in both solution- and droplet-to-iron electrochemical reaction simulations. Second, solution- and droplet-to-iron electrochemical reaction simulations reflect the passivation film formation and dissolution processes. Third, the mechanism of charge transfer and the formation of built-in electric fields in droplet-to-iron electrochemical reaction are explored. The hydroxyl radicals that penetrated the ordered structure acquire electrons from the iron atoms on the substrate surface under the action of Coulomb forces and form iron-containing oxides with these iron atoms. Hydroxyl radicals left in the ordered structure and positively charged iron atoms that have lost electrons on the substrate surface form a built-in electric field. The formation of the built-in electric field is the way electron transfer is presented. Fourth, the effect of wetting on corrosion and the effect of postcorrosion on wetting are investigated. However, the coupling process has been rarely investigated in solution-to-metal electrochemical reaction studies by other scholars.

3.2. Impact of Different Parameters on Droplet-to-Iron Electrochemical Reaction.

3.2.1. Effect of Temperature. Figure 6 shows the effect of temperatures on droplet-to-iron electrochemical reaction at 2.5 MV/cm and 8.69 M. This figure also shows the time plot from 30 ps to the first appearance of corrosion. A comparison of the second column of Figure 6a and c reveal that the water molecules shown in

https://doi.org/10.1021/acsomega.4c01236
ACS Omega 2024, 9, 20410−20424

Table 2. Comparison of Other Studies to This Work

Comparison	Schematics	Essential points
Model application	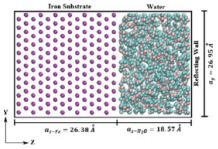	Solution and pure iron substrate are modeled in solution-to-metal electrochemical reaction (25).
	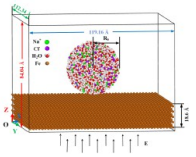	Droplet and pure iron substrate are modeled in droplet-to-iron electrochemical reaction.
Electrochemical reaction	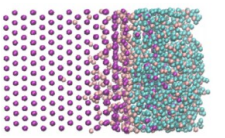	Solution-to-metal electrochemical reaction involves the formation and dissolution of passivation films (25).
	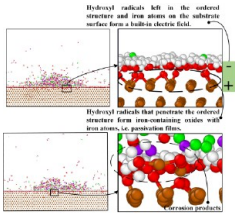	① Droplet wets the iron first in droplet-to-iron electrochemical reaction. (See Figure 2 for details of the wetting process.) ② Droplet-to-iron electrochemical reaction also involves the formation and dissolution of passivation films.
Charge transfer mechanism	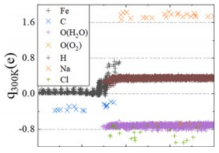	The structure of the substrate causes the carbon steel surface to be positively charged (17), but the mechanism of charge transfer is not revealed.
	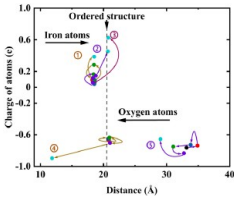	① The process of charge change of iron and oxygen atoms and the mechanism of charge transfer are revealed in droplet-to-iron electrochemical reaction. ② The formation of the built-in electric field is revealed.
Coupling process	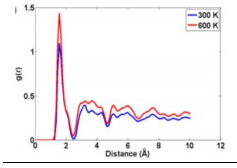	Wetting is rarely considered in solution-to-metal electrochemical reaction (18).
	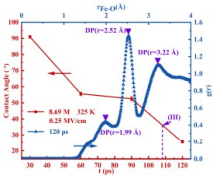	Droplet-to-iron electrochemical reaction is a coupling process of wetting and corrosion. The effects of wetting on corrosion and the post-corrosion on wetting are considered.

Figure 6c have a wider diffusion in the environment and a more significant number. Increasing the temperature increases the percentage of activated water molecules, and more effective collisions occur between water molecules. As a result, water molecules are more likely to detach from the droplet and spread more widely at higher temperatures.

Figure 7 shows the number of bonds formed between hydroxyl radicals penetrating the ordered structure and the iron substrate inside the solid box in the third column of Figure 6. The number of bonds in Figure 7 clearly shows that the number of iron-containing oxides increases with increasing temperature. The increase in the temperature decreases the intermolecular forces in the droplet. Thus, the droplet viscosity decreases, as confirmed by Rizza et al.[43] The reduction in viscosity results in lower resistance to particle motion in the droplet. Therefore, particle collisions with hydroxyl radicals in the ordered structure are more likely to occur. A high temperature corresponds to increased penetration of the hydroxyl radicals into the ordered structure to form bonds with iron atoms. At the same time, the time required to form bonds is drastically reduced.

The variation of contact angle from 30 to 90 ps at different temperatures is shown in Figure 8. The contact angle first decreases rapidly. As wetting progresses, the decrease gradually slows down. However, the electrochemical reaction enters the third stage at 80 ps at a temperature of 350 K. The formation of corrosion products and craters accelerates the contact angle decrease. Therefore, the decrease rate of the contact angle at 350 K is higher than that at 300 and 325 K, as shown in arrow (III) in Figure 8a.

Figure 8b shows charge and position changes for several steps at 325 K. Iron atoms dissolve into the ordered structure with a charge of about 0.5 *e*. The dissolved iron atoms are in the third stage of the electrochemical reaction and exhibit a cyan color. Appearing successively under the cyan-colored area are purple, green, and blue, representing different time steps in the second stage of the electrochemical reaction. The overlapping colors indicate no change in the atomic position or charge. The black and red colors represent two different time steps in the first stage of electrochemical reaction, when the iron atoms have a charge of approximately 0 *e*. Figure 8b indicates that the charge amount of iron atoms shows an overall increasing trend as electrochemical reaction.

The three close-up snapshots in Figure 9a, b, and c are the grid views at the same simulation time under different temperatures. From the span of corrosion crater distribution, a high temperature corresponds to a more extensive droplet wetting on the iron substrate surface and, thus, a larger corrosion crater. By contrast, only pitting appears at lower temperatures. Excellent mass transfer properties enable the evaluation of efficient electrochemical reactions. Mass transfer performance refers to the process of transferring substances between different phases, and currently, the contact angle measures a system's wetting state and mass transfer performance.[44,45] In electrochemical systems, the mass transfer performance is manifested by the movement of charged particles under an electric field. Figure 9d and e evaluate the mass transfer performance. The number of iron atoms that penetrated the droplet and the number of oxygen atoms (from the hydroxyl radical) that penetrated the iron substrate are shown in Figure 9d and e. The penetration of atoms is a microscopic manifestation of corrosion. As seen in Figure 9d and e, earlier penetration of atoms and a larger penetration atom number at a higher temperature indicate the earlier occurrence of corrosion and a larger corrosion crater. This result further confirms from a microscopic perspective that increasing the temperature can promote corrosion.

3.2.2. Effect of Electric Field Strength. Figure 10 shows the effect of electric field strength on droplet-to-iron electrochemical reaction at 300 K and 8.69 M. A comparison of the second columns of Figure 10a and c shows that the droplet height decreases continuously as the electric field strength

https://doi.org/10.1021/acsomega.4c01236
ACS Omega 2024, 9, 20410−20424

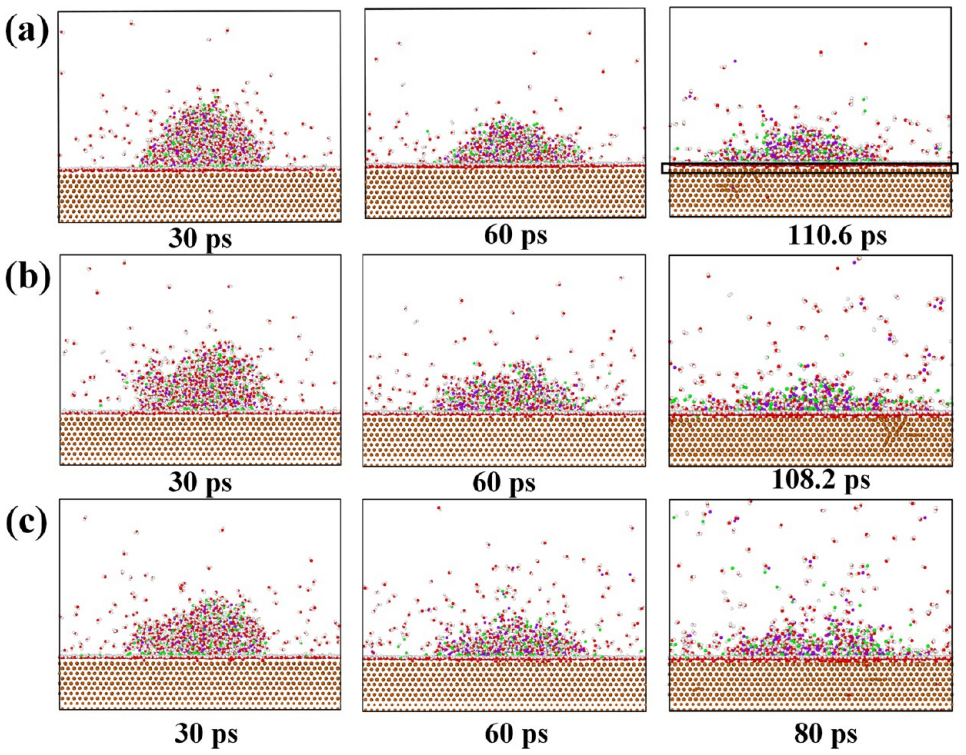

Figure 6. Snapshots of electrochemical reaction at different temperatures: (a) 300 K, (b) 325, and (c) 350 K.

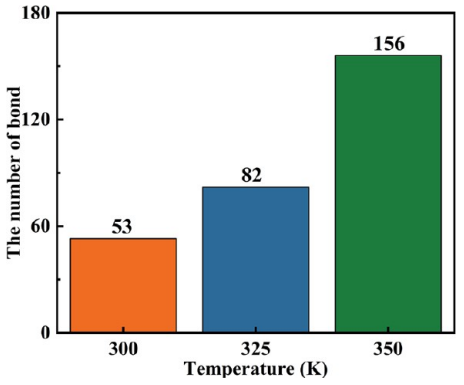

Figure 7. Number of bonds formed between hydroxyl radicals and iron atoms at different temperatures.

increases, as shown by the more wetted droplet in Figure 10c. A strong electric field corresponds to increased dissociation of the water molecules in the droplet.[46] Then, more hydroxyl radicals are produced and move faster toward the iron substrate under a high electric field strength, which is the reason for the decrease in the droplet height. A comparison of the third columns of Figure 10a and c show that more water molecules evaporate into the environment in Figure 10a than in Figure 10c. Relatively fewer water molecules are retained in the droplet in Figure 10a. A positive relationship is known to exist between evaporation and the contact area of the water droplet. A more significant contact area corresponds to intense droplet evaporation. When the water molecules in the droplet are reduced, the water molecules in contact with the environment will naturally be reduced, and the evaporated

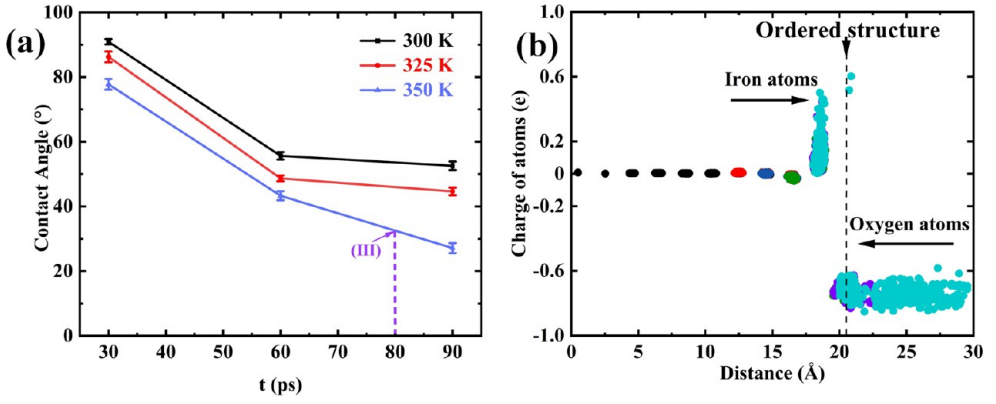

Figure 8. (a) Variation of droplet contact angle with time at different temperatures. (b) Charge and position changes of iron and oxygen atoms with time at 325 K. Electrochemical reaction stage 1: black and red. Electrochemical reaction stage 2: blue, green, and purple. Electrochemical reaction stage 3: cyan.

https://doi.org/10.1021/acsomega.4c01236
ACS Omega 2024, 9, 20410−20424

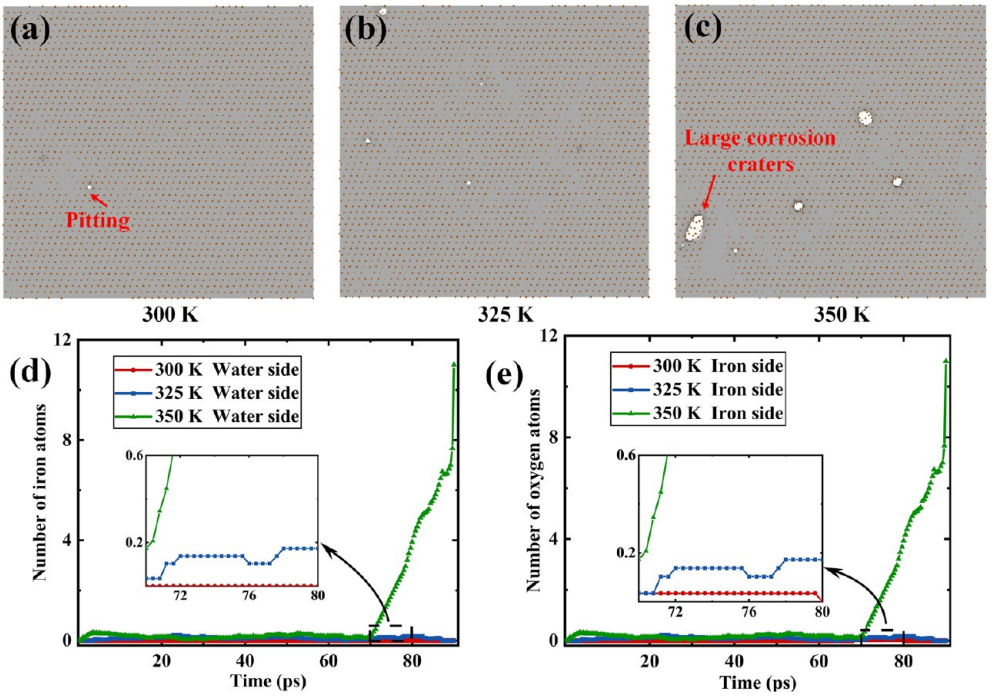

Figure 9. Close-up snapshots of the iron substrate surface network at (a) 300 K, (b) 325, and (c) 350 K. Number of penetrated (d) iron atoms and (e) oxygen atoms at different temperatures over time.

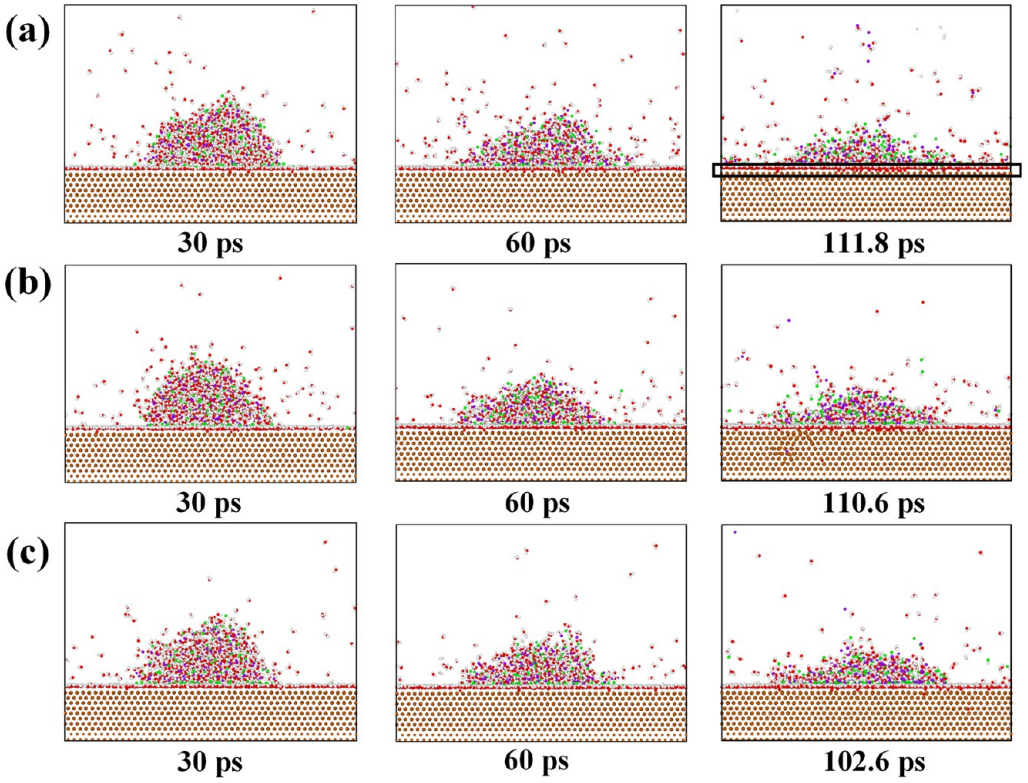

Figure 10. Snapshots of electrochemical reaction at different electric field strengths: (a) 2, (b) 2.5, and (c) 3 MV/cm.

water molecules will be reduced, which is why water molecules evaporate less under a high electric field strength.

Figure 11 shows that as the electric field strength increases, the number of formed bonds decreases, indicating a decrease in the number of iron-containing oxides. However, from the third column of Figure 10, the time for electrochemical reaction occurrence decreases with the increase in the electric field strength. The dissociated hydroxyl radicals are subjected to high electric field strengths and have fewer collisions with the surrounding particles (constrained by the strong electric field force), thus, decreasing kinetic energy. Hydroxyl radicals with reduced kinetic energy cannot penetrate the ordered

https://doi.org/10.1021/acsomega.4c01236
ACS Omega 2024, 9, 20410−20424

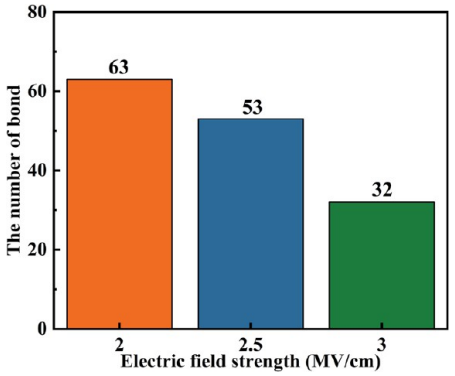

Figure 11. Number of bonds formed between hydroxyl radicals and iron atoms at different electric field strengths.

structure, so the stronger the electric field strength, the fewer bonds are formed. The stronger the electric field strength, the more water dissociates, but that does not mean that the hydroxyl radicals in the droplet can form a bond with the iron. After being subjected to particle collisions, the bond will be formed only when the hydroxyl radicals reach a kinetic energy capable of penetrating the ordered structure. The electric field strength will constrain particle collision, but it will shorten the time for the high kinetic energy hydroxyl radicals to penetrate the ordered structure.

As shown in Figure 12a, the decay rate of the contact angle is larger at 30−60 ps and smaller at 60−90 ps. The larger decay rate at 30−60 ps is because the hydroxyl radicals have not yet fully covered the metal surface and are in a wetting process. However, the lower decay rate at 60−90 ps may be since a dense ordered structure occupies the iron surface, the wetting rate of the droplets will gradually slow down, and the rate of the contact angle decrease will also decrease.

The charge distribution is shown in Figure 12b, which also demonstrates the phenomenon where iron atoms on the surface of the iron substrate are more positively charged than those in the interior of the iron substrate. This phenomenon further confirms the formation of the built-in electric field, which is the way that the electron transfer is presented.

Figure 13a−c shows that corrosion craters formed at different electric field strengths. A high electric field strength corresponds to a large corrosion crater at the beginning of the corrosion. The number of penetrated atoms is displayed in Figure 13d and e. A high electric field strength is usually considered to correspond to more hydroxyl radicals penetrating the ordered structure. The uncommon findings in Figure 13 can be explained by the effect of electric field strength. A high electric field strength results in a high electric field force applied to the particle, thus restricting the free movement of particles and reducing the effective collisions with hydroxyl radicals and inhibiting the number of hydroxyl radicals penetrating the ordered structure. In summary, a high electric field strength corresponds to a smaller number of hydroxyl radicals penetrating the ordered structure. The number of penetrated iron and oxygen atoms shows a trend of first increasing and then stabilizing at 2.5 and 3 MV/cm in the investigated time range, which also indicates a convergence process in forming corrosion craters. A high electric field strength corresponds to an earlier increase in the number of penetrated atoms and a smaller number of penetrated atoms. Therefore, a high electric field strength corresponds to earlier formation of the corrosion crater but also a smaller number of penetrated atoms in Figure 13d and e. This result is consistent with the phenomena in Figure 11 and the third column of Figure 10.

3.2.3. Effect of salt concentration. Figure 14 presents the effect of salt concentration on droplet-to-iron electrochemical reaction at 300 K and 2.5 MV/cm. The effect of electric field strength has been studied in Section 3.2.2, and the droplet can maintain its morphology at different electric field strengths at a salt concentration of 8.69 M. Therefore, a high electric field strength is not the reason the droplet cannot maintain its morphology. At 0.77 M, water molecules have difficulty maintaining the droplet morphology after 30 ps, and many water molecules are present in the environment. A high concentration corresponds to a greater electrostatic attraction between anions and sodium ions in the droplet. Thus, the droplet can easily maintain its morphology, indicating that a high salt concentration is beneficial for maintaining the droplet morphology. This condition is also demonstrated by the wetting of metal surfaces by droplets of different concentrations as studied by Li et al.[47] Li et al. found that a high concentration corresponds to a high contact angle, which not only indicates that maintaining the droplet morphology at low concentrations is more challenging but that it also coincides with the contact angle in Figure 16a. Additionally, the effect of salt concentration on electrochemistry is reflected in the fact that the ions promote the dissociation of water, as illustrated in the first-principles used by Chen et al.,[48] where two hydroxyl

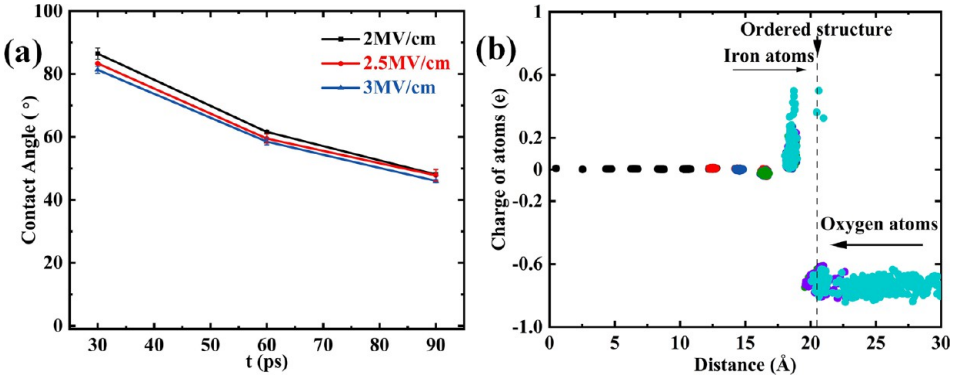

Figure 12. (a) Variation of the droplet contact angle with time at different electric field strengths. (b) Charge and position changes of iron and oxygen atoms with time at 2.5 MV/cm. Electrochemical reaction stage 1: black and red. Electrochemical reaction stage 2: blue, green, and purple. Electrochemical reaction stage 3: cyan.

https://doi.org/10.1021/acsomega.4c01236
ACS Omega 2024, 9, 20410−20424

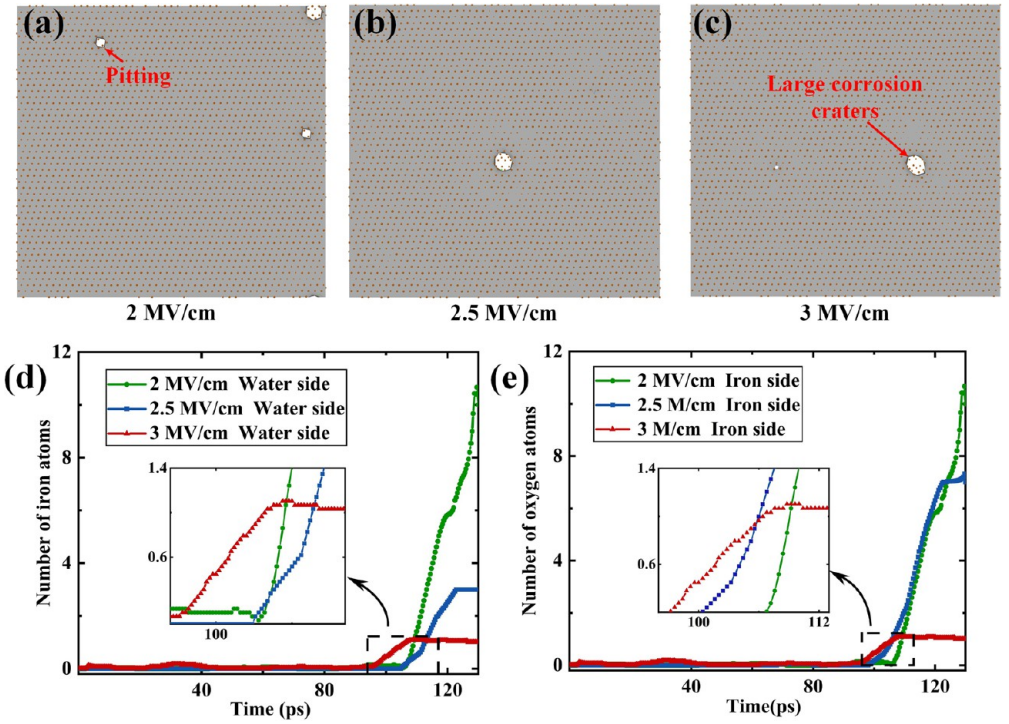

Figure 13. Close-up snapshots of the iron substrate surface network at (a) 2 MV/cm, (b) 2.5 MV/cm, and (c) 3 MV/cm. Number of penetrated (d) iron atoms and (e) oxygen atoms at different electric field strengths over time.

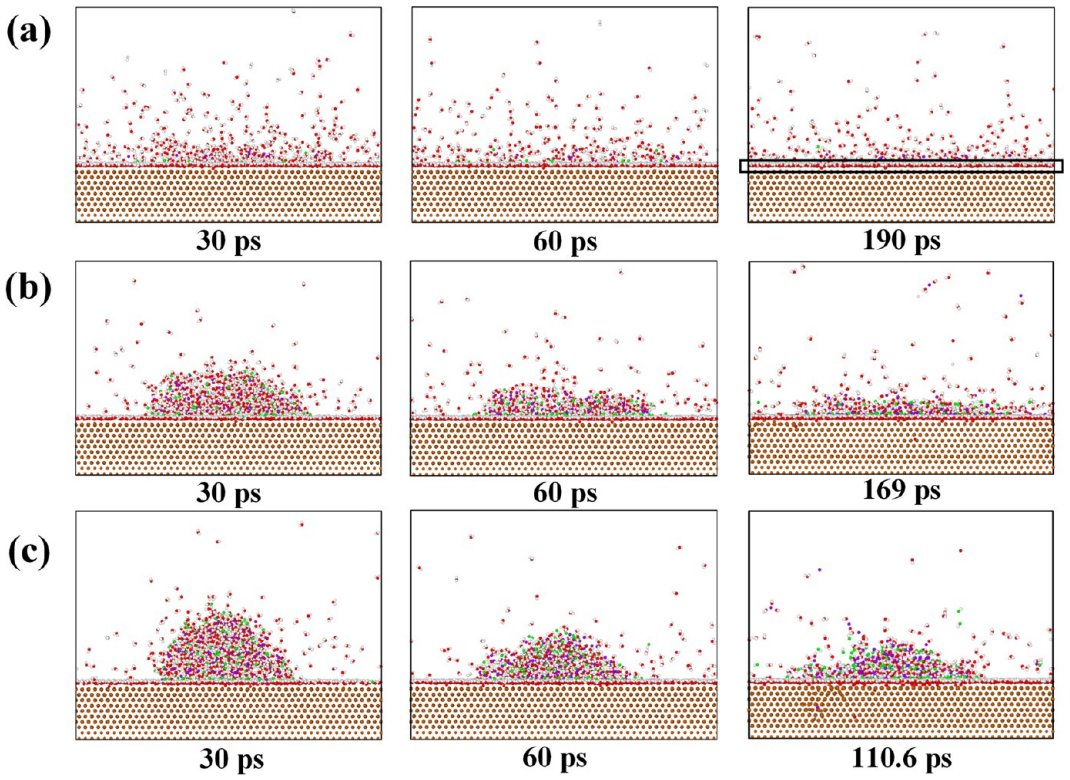

Figure 14. Snapshots of electrochemical reaction at different salt concentrations: (a) 0.77, (b) 4.73 and (c) 8.69 M.

radicals can induce the dissociation of a single water molecule in the presence of chloride ions.

Figure 15 and the third column of Figure 14 show that the number of iron-containing oxides increases and the time for electrochemical reaction occurrence decreases with the increase in the salt concentration. This phenomenon may be caused by the higher the droplet salt concentration, the stronger the electrostatic attraction and the more the particles are confined in the droplet, leading to an increased likelihood of collision of the particles in the droplet. Although the low-concentration droplet wets to a high degree, it spreads only out on the iron surface and forms an ordered structure. Because

https://doi.org/10.1021/acsomega.4c01236
ACS Omega 2024, 9, 20410−20424

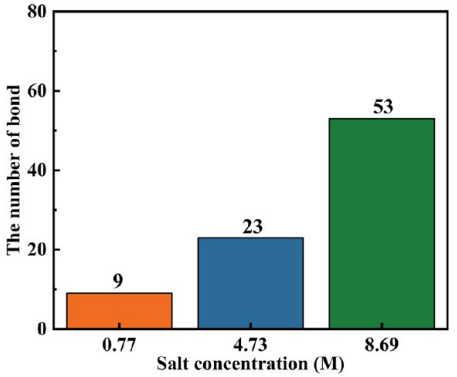

Figure 15. Number of bonds formed between hydroxyl radicals and iron atoms at different salt concentrations.

the low-concentration particles are more dispersed in the system, there are fewer collisions of the particles with the hydroxyl radicals to the point where the hydroxyl radicals do not have enough kinetic energy to penetrate the ordered structure. Hydroxyl radicals with sufficiently large kinetic energy can penetrate the ordered structure and thus form bonds. The effect of concentration is to make collisions of particles with hydroxyl radicals more possible.

As shown in Figure 16a, the contact angle finally tends to 0° at the concentration of 0.77 M because water molecules diffuse to the environment. As the concentration increases from 4.73 to 8.69 M, the decrease rate of the contact angle shows a trend of first increasing from 30 to 60 ps and then decreasing from 60 to 90 ps. This result is similar to the effect of electric field strength on the contact angle as discussed in Section 3.2.2, indicating that the increase in salt concentration generates a more densely single-molecular-layer ordered structure.

In addition to the contact angle, charge and position changes are investigated in Figure 16b. The other colors under the cyan portion indicate no atomic position or charge change. A non-overlapping portion of purple and cyan colors appears on the oxygen atom side. The purple oxygen atoms on the left side of the ordered structure are iron-containing oxides, i.e., the passivation film. The purple atom enters the single-molecular-layer ordered structure at the next time step (represented in cyan). The purple-to-cyan process indicates the dissolution process of the passivation film.

As can be seen from the corrosion craters in Figures. 17a, b, and c, a high salt concentration corresponds to an increased likelihood to produce large corrosion craters, whereas pitting does not even occur at low concentrations. A high salt concentration corresponds to a greater effect of Coulomb forces on the chloride ions. The effective collisions between particles will also increase, and the damage to the single-molecular-layer ordered structure will be greater. Once the local single molecular layer is destroyed, the corrosion rate will be accelerated (Figures. 17d, e). The appearance of corrosion craters promotes droplet wetting, as mentioned in Section 3.1. This result not only coincides with the viewpoint of Caceres et al.,[49] who found that a high concentration of chloride ions is required to cause pitting, but also mirrors the findings of Jeon et al.,[16] who stated that 5 M NaCl solution is a high concentration. As seen in Figures. 17d and e, a high salt concentration corresponds to less time required for the corrosion and the increased penetration of iron atoms and oxygen atoms into the droplet and iron interface.

4. CONCLUSION

In this work, the electrochemical reaction of droplet-to-iron is investigated through reactive molecular dynamics simulations, and a simulation model for the droplet-to-iron electrochemical reaction is developed for the first time. The factors that affect the electrochemical reactions are studied. The variations in contact angle and products during the electrochemical reaction are analyzed. Charge and atomic position changes are tracked, and the extension of the dissolved region on the iron surface is recorded. The number of atoms in the different phases is counted. On the basis of the simulation results and the corresponding analysis, the following conclusions are obtained:

(1) The droplet-to-iron electrochemical reaction is divided into three stages. First, water molecules, dissociated hydroxyl radicals, and hydrogen ions spread out on the iron surface to form a single-molecular-layer ordered structure. In the ordered structure, the oxygen atoms face toward the iron, while the hydrogen atoms move away from the iron. Second, the hydroxyl radicals in the ordered structure are subjected to electric field force and Coulomb force and collide with particles. Some hydroxyl radicals that accumulate enough energy can penetrate the ordered structure and form iron-containing oxides with iron atoms. Finally, the hydroxyl radicals pull the

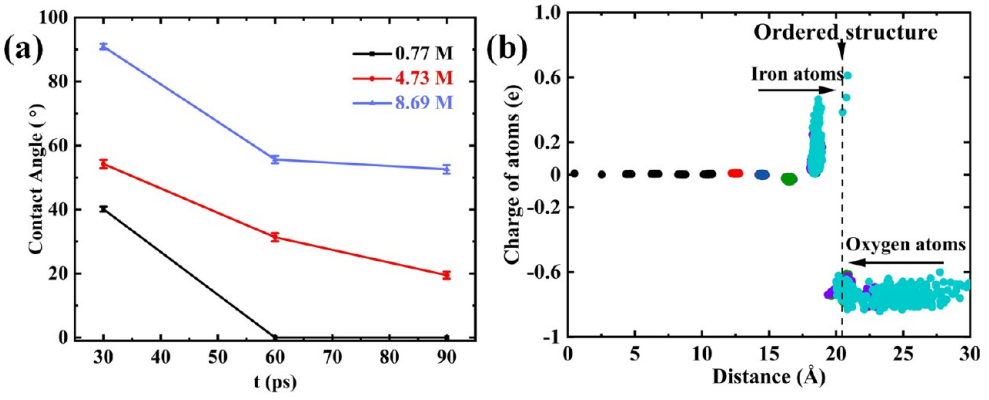

Figure 16. (a) Variation of droplet contact angle with time at different salt concentrations. (b) Charge and position changes of iron and oxygen atoms with time at 4.73 M. Electrochemical reaction stage 1: black and red. Electrochemical reaction stage 2: blue, green, and purple. Electrochemical reaction stage 3: cyan.

https://doi.org/10.1021/acsomega.4c01236
ACS Omega 2024, 9, 20410−20424

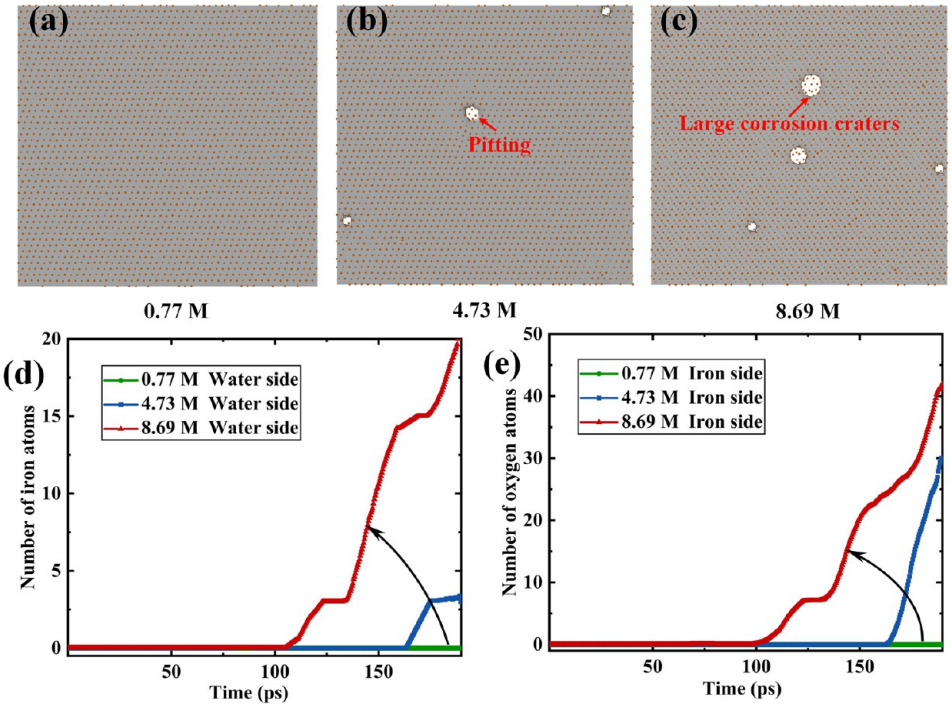

Figure 17. Close-up snapshots of the iron substrate surface network at (a) 0.77 4.73, and (c) 8.69 M. Number of penetrated (d) iron atoms and (e) oxygen atoms at different salt concentrations.

iron atoms from the surface of the iron substrate. The initial formation of pitting causes the originally compact iron to become loose, which enlarges the contact area between the hydroxyl radicals and the iron and further accelerates the development of pitting to large corrosion craters.

(2) Wetting (the droplet spreading on the iron surface) and corrosion (the chemical reaction between the droplet and the iron) are coupled in the electrochemical reaction of droplet-to-iron. The formation of a single-molecular-layer ordered structure is a prerequisite for corrosion to occur. In turn, droplet-to-iron electrochemical reaction will affect the droplet wetting. Corrosion products in the droplet reduce the interaction within the droplet. Accompanying the formation of corrosion products, corrosion craters result in larger areas of the iron surface coming into contact with hydroxyl radicals. The corrosion products and craters promote the further wetting of droplet and the spreading of the single-molecular-layer ordered structure on the iron surface. The spreading also intensifies the corrosion.

(3) Increases in temperature, electric field strength, and concentration promote electrochemical reaction, further accelerating droplet wetting. Temperature strengthens electrochemical reaction by increasing the effective collisions with hydroxyl radicals. A high electric field strength corresponds to a greater electric field force acting on the particles moving toward the substrate, which accelerates the movement of particles toward the substrate but reduces the effective collisions with hydroxyl radicals. Therefore, electrochemical reaction occurs earlier, but fewer hydroxyl radicals penetrate the ordered structure. In addition, the effect of concentration on the electrochemical reaction is reflected in the chloride ions. The large corrosion crater is caused by a high concentration of chloride ions. A high chloride ion concentration corresponds to a stronger attack of the chloride ions, thus destroying the single-molecular-layer ordered structure. Chloride ions also promote the dissociation of water. However, the corrosion craters do not expand infinitely but rather corrode with new pitting. The evolution of the corrosion crater is divided into three processes: derivation, development, and convergence.

AUTHOR INFORMATION

Corresponding Author

Hang Dong − *School of Mechanical Engineering, Xinjiang University, Urumqi 830046, China;* orcid.org/0009-0004-5704-268X; Email: donghangxju@163.com

Authors

Can Zhao − *School of Mechanical Engineering, Xinjiang University, Urumqi 830046, China*

Na Kong − *Xinjiang Uygur Autonomous Region Science and Technology Project Service Center, Urumqi 830011, China*

Yu Zhou − *State Key Laboratory of Mechanical System and Vibration, School of Mechanical Engineering, Shanghai Jiao Tong University, Shanghai 200240, China*

Jianping Zhou − *School of Mechanical Engineering, Xinjiang University, Urumqi 830046, China*

Complete contact information is available at: https://pubs.acs.org/10.1021/acsomega.4c01236

Notes

The authors declare no competing financial interest.

ACKNOWLEDGMENTS

This research is sponsored by the Key Research and Development Projects of Xinjiang Uygur Autonomous Region

https://doi.org/10.1021/acsomega.4c01236
ACS Omega 2024, 9, 20410−20424

(2023B01016-2), the Natural Science Foundation of Xinjiang Uygur Autonomous Region (Grant No. 2022D01C672), the Special Funds for Local Science and Technology Development under the Guidance of the Central Government (Grant No. ZYYD2023A07), the National Natural Science Foundation of China (Grant No. 52105486, 52265061), the China Postdoctoral Science Foundation (Grant No. 2020M683612, 2022T150551), the Doctoral Research Initiation Fund Project of Xinjiang University, the Tianchi Doctoral Project of Xinjiang Uyghur Autonomous Region (Grant No. TCBS202019).

REFERENCES

(1) Sundaram, R. G.; Vengatesh, G.; Sundaravadivelu, M. Surface morphological and quantum chemical studies of some expired drug molecules as potential corrosion inhibitors for mild steel in chloride medium[J]. *Surfaces and Interfaces* **2021**, *22*, 100841.

(2) Renner, F. U.; Stierle, A.; Dosch, H.; et al. Initial corrosion observed on the atomic scale[J]. *Nature* **2006**, *439* (7077), 707−710.

(3) Syed, J. A.; Tang, S.; Meng, X. Super-hydrophobic multilayer coatings with layer number tuned swapping in surface wettability and redox catalytic anti-corrosion application[J]. *Sci. Rep.* **2017**, *7* (1), 4403.

(4) Li, F. M.; Huang, L.; Zaman, S.; et al. Corrosion chemistry of electrocatalysts[J]. *Adv. Mater.* **2022**, *34*, 2200840.

(5) Noorbakhsh Nezhad, A. H.; Arefinia, R.; Kashefi, M.; Davoodi, A.; Hosseinpour, S.; et al. Compatibility of fabrication of super-hydrophobic surfaces and addition of inhibitors in designing corrosion prevention strategies for electrodeposited nickel in saline solutions[J]. *Appl. Surf. Sci.* **2019**, *493*, 1243−1254.

(6) Dong, H.; Liu, Y.; Li, M.; et al. Experimental investigation of water-in-oil nanoemulsion in sinking electrical discharge machining-[J]. *Materials and Manufacturing Processes* **2019**, *34* (10), 1129−1135.

(7) Bi, P.; Li, H.; Zhao, G.; et al. Robust super-hydrophobic coating prepared by electrochemical surface engineering for corrosion protection[J]. *Coatings* **2019**, *9* (7), 452.

(8) Webb, E. B.; Grest, G. S.; Heine, D. R.; Hoyt, J.J.; et al. Dissolutive wetting of Ag on Cu: A molecular dynamics simulation study[J]. *Acta Mater.* **2005**, *53* (11), 3163−3177.

(9) Boyer, H. E.; Gall, T. L. . *Metals Handbook: Desk Edition*; ASTM International, 1985.

(10) Mookam, N.; Kanlayasiri, K. Influences of soldering time on wettability and intermetallic phase between Sn-3.0 Cu solder and copper substrate[C]//MATEC Web of Conferences. *EDP Sciences* **2018**, *192*, 01024.

(11) Sempels, W.; De Dier, R.; Mizuno, H.; et al. Auto-production of biosurfactants reverses the coffee ring effect in a bacterial system[J]. *Nat. Commun.* **2013**, *4* (1), 1757.

(12) Deen, J.; Sempels, W.; De Dier, R.; et al. Combing of genomic DNA from droplets containing picograms of material[J]. *ACS Nano* **2015**, *9* (1), 809−816.

(13) Li, M.; Wu, S.; Wang, P.; et al. Molecular progress of the corrosion of passivated Iron: The effects of structural strain[J]. *Construction and Building Materials* **2022**, *360*, 129537.

(14) Assowe, O.; Politano, O.; Vignal, V.; et al. Reactive molecular dynamics of the initial oxidation stages of Ni (111) in pure water: effect of an applied electric field[J]. *J. Phys. Chem. A* **2012**, *116* (48), 11796−11805.

(15) Jeon, B.; Sankaranarayanan, S. K. R. S.; Van Duin, A. C. T.; et al. Atomistic insights into aqueous corrosion of copper[J]. *J. Chem. Phys.* **2011**, *134* (23), 234706.

(16) Jeon, B.; Sankaranarayanan, S. K. R. S.; Van Duin, A. C. T.; et al. Reactive molecular dynamics study of chloride ion interaction with copper oxide surfaces in aqueous media[J]. *ACS Appl. Mater. Interfaces* **2012**, *4* (3), 1225−1232.

(17) Du, L.; Chen, J.; Hu, E.; et al. A reactive molecular dynamics simulation study on corrosion behaviors of carbon steel in salt spray[J]. *Comput. Mater. Sci.* **2022**, *203*, 111142.

(18) Subbaraman, R.; Deshmukh, S. A.; Sankaranarayanan, S K R S. Atomistic insights into early stage oxidation and nanoscale oxide growth on Fe (100), Fe (111) and Fe (110) surfaces[J]. *J. Phys. Chem. C* **2013**, *117* (10), 5195−5207.

(19) Farzi, N.; Hydarifard, M. H.; Izadi, M. E.; et al. Investigation of iron carbide (Fe_3C) corrosion in water and acidic solution using ReaxFF molecular dynamics[J]. *J. Mol. Liq.* **2020**, *318*, 114006.

(20) Huang, Y.; Hu, C.; Xiao, Z.; et al. Atomic insight into iron corrosion exposed to supercritical water environment with an improved Fe-H_2O reactive force field[J]. *Appl. Surf. Sci.* **2022**, *580*, 152300.

(21) Chenoweth, K.; Van Duin, A. C. T.; Goddard, W. A. ReaxFF reactive force field for molecular dynamics simulations of hydrocarbon oxidation[J]. *J. Phys. Chem. A* **2008**, *112* (5), 1040−1053.

(22) Rappe, A. K.; Goddard, W. A. Charge equilibration for molecular dynamics simulations[J]. *J. Phys. Chem.* **1991**, *95* (8), 3358−3363.

(23) Aryanpour, M.; van Duin, A. C. T.; Kubicki, J. D. Development of a reactive force field for iron− oxyhydroxide systems[J]. *J. Phys. Chem. A* **2010**, *114* (21), 6298−6307.

(24) Rahaman, O.; Van Duin, A. C. T.; Bryantsev, V. S.; et al. Development of a ReaxFF reactive force field for aqueous chloride and copper chloride[J]. *J. Phys. Chem. A* **2010**, *114* (10), 3556−3568.

(25) DorMohammadi, H.; Pang, Q.; Árnadóttir, L.; et al. Atomistic simulation of initial stages of iron corrosion in pure water using reactive molecular dynamics[J]. *Comput. Mater. Sci.* **2018**, *145*, 126−133.

(26) DorMohammadi, H.; Pang, Q.; Murkute, P.; et al. Investigation of chloride-induced depassivation of iron in alkaline media by reactive force field molecular dynamics[J]. *npj Materials Degradation* **2019**, *3* (1), 19.

(27) Psofogiannakis, G. M.; McCleerey, J. F.; Jaramillo, E.; et al. ReaxFF reactive molecular dynamics simulation of the hydration of Cu-SSZ-13 zeolite and the formation of Cu dimers[J]. *J. Phys. Chem. C* **2015**, *119* (12), 6678−6686.

(28) Martínez, J. M.; Martínez, L. Packing optimization for automated generation of complex system's initial conFigureurations for molecular dynamics and docking[J]. *Journal of computational chemistry* **2003**, *24* (7), 819−825.

(29) Thompson, A. P.; Aktulga, H. M.; Berger, R.; et al. LAMMPS-a flexible simulation tool for particle-based materials modeling at the atomic, meso, and continuum scales[J]. *Comput. Phys. Commun.* **2022**, *271*, 108171.

(30) Stukowski, A. Visualization and analysis of atomistic simulation data with OVITO−the Open Visualization Tool[J]. *Modell. Simul. Mater. Sci. Eng.* **2010**, *18* (1), 015012.

(31) Dong, H.; Liu, Y.; Zhou, Y.; et al. Mechanism investigation of coalescence behaviors of conducting droplets by molecular dynamics simulations[J]. *Colloids Surf., A* **2019**, *570*, 55−62.

(32) Zhou, Y.; Dong, H.; Liu, Y. H.; et al. Molecular dynamics simulations of the electrocoalescence behaviors of two unequally sized conducting droplets[J]. *Langmuir* **2019**, *35* (20), 6578−6584.

(33) Song, H.; Lee, Y.; Jin, S.; et al. Prediction of sessile drop evaporation considering surface wettability[J]. *Microelectron. Eng.* **2011**, *88* (11), 3249−3255.

(34) Wu, X.; Yang, Z.; Duan, Y. Molecular dynamics simulation on evaporation of a suspending difluoromethane nanodroplet[J]. *Int. J. Heat Mass Transfer* **2020**, *158*, 120024.

(35) Suganuma, Y.; Yamamoto, S.; Kinjo, T.; et al. Wettability of Al2O3 surface by organic molecules: insights from molecular dynamics simulation[J]. *J. Phys. Chem. B* **2017**, *121* (42), 9929−9935.

(36) Li, C. Y.; Le, J. B.; Wang, Y. H.; et al. In situ probing electrified interfacial water structures at atomically flat surfaces[J]. *Nature materials* **2019**, *18* (7), 697−701.

(37) Wang, Y. H.; Zheng, S.; Yang, W. M.; et al. In situ Raman spectroscopy reveals the structure and dissociation of interfacial water[J]. *Nature* **2021**, *600* (7887), 81−85.

(38) Jung, S.; Suh, D.; Yoon, W. Molecular dynamics simulation on the energy exchanges and adhesion probability of a nano-sized particle

https://doi.org/10.1021/acsomega.4c01236
ACS Omega 2024, 9, 20410−20424

colliding with a weakly attractive static surface[J]. *J. Aerosol Sci.* **2010**, *41* (8), 745−759.
(39) Lin, S.; Chen, X.; Wang, Z. L. Contact electrification at the liquid−solid interface[J]. *Chem. Rev.* **2022**, *122* (5), 5209−5232.
(40) Hastuty, S.; Nishikata, A.; Tsuru, T. Pitting corrosion of Type 430 stainless steel under chloride solution droplet[J]. *Corros. Sci.* **2010**, *52* (6), 2035−2043.
(41) Liu, W.; Ao, S.; Li, Y.; et al. Effect of anodic behavior on electrochemical machining of TB6 titanium alloy[J]. *Electrochim. Acta* **2017**, *233*, 190−200.
(42) Pan, T. Quantum chemistry-based study of iron oxidation at the iron−water interface: An X-ray analysis aided study[J]. *Chem. Phys. Lett.* **2011**, *511* (4−6), 315−321.
(43) Rizza, M. A.; Wijayanti, W.; Hamidi, N.; et al. Role of Intermolecular forces on the contact angle of vegetable oil droplets during the cooling process[J]. *Scientific World Journal, 2018* **2018**, *2018*, 1.
(44) Xie, L.; Wang, L.; Zhao, W.; et al. WS2 moiré superlattices derived from mechanical flexibility for hydrogen evolution reaction[J]. *Nat. Commun.* **2021**, *12* (1), 5070.
(45) Xie, L.; Wang, L.; Liu, X.; et al. Tetra-Coordinated W2S3 for Efficient Dual-pH Hydrogen Production[J]. *Angew. Chem., Int. Ed.* **2024**, *63* (5), No. e202316306.
(46) Saitta, A. M.; Saija, F.; Giaquinta, P. V. Ab initio molecular dynamics study of dissociation of water under an electric field[J]. *Physical review letters* **2012**, *108* (20), 207801.
(47) Li, X.; Zhang, C.; Wang, J.; et al. Atomic-level insights into nano-salt droplets wetting on the MgO surface using molecular dynamics simulations[J]. *Corros. Sci.* **2020**, *167*, 108549.
(48) Chen, B.; Zhang, C. H.; Jin, Y. The roles of Cl− and OH− in the dissociation of H2O molecules on an Al surface: A first-principles calculation[J]. *J. Phys. Chem. Solids* **2021**, *159*, 110281.
(49) Cáceres, L.; Vargas, T.; Herrera, L. Influence of pitting and iron oxide formation during corrosion of carbon steel in unbuffered NaCl solutions[J]. *Corrosion science* **2009**, *51* (5), 971−978.

https://doi.org/10.1021/acsomega.4c01236
ACS Omega 2024, 9, 20410−20424